# Test and evaluation of a simple parameterization to enhance air-sea coupling in a global coupled model

**Fanghua Xu[1]**

[1] Ministry of Education Key Laboratory for Earth System Modeling, and Department of Earth System Science, Tsinghua University, Beijing, China

* Corresponding Author: fxu@tsinghua.edu.cn

**Abstract:** A simple temperature-dependent wind stress scheme is implemented in National Center for Atmospheric Research (NCAR) Community Earth System Model (CESM), aiming to enhance positive wind stress and sea surface temperature (SST) correlation in SST-frontal regions. A series of three-year coupled experiments are conducted to determine a proper coupling coefficient for the scheme based on the agreement of surface wind stress and SST at oceanic mesoscale between model simulations and observations. Afterwards, 80-year simulations with/without the scheme are conducted to explore its effects on simulated ocean states and variability. The results show that the new scheme indeed improves the positive correlation between SST and wind stress magnitude near the large oceanic fronts. With more realistic surface heat flux and wind stress, the global SST biases are reduced. The global ocean circulation represented by barotropic stream function exhibits a weakened gyre circulation close to the western boundary separation, in agreement with previous studies. The simulation of equatorial Pacific current system is improved as well. The overestimated El Niño Southern Oscillation (ENSO) magnitude in original CESM is reduced by ~30% after using the new scheme with an improved period.

*Keywords:* SST front; Air-sea interaction; Wind stress; CESM

## 1. Introduction

The sea surface temperature (SST) frontal influences on surface winds and wind stress at oceanic mesoscale have been well documented[1–10]. Satellite scatterometer measurements, in-situ observations and numerical models all reveal that surface wind is higher over warm water and lower over cold water near a SST front. Wind blowing across the SST front generates divergence, and wind blowing parallel to the front generates curl[7]. Subsequently, wind stress divergence is proportional to downwind SST gradients, and wind stress curl is proportional to crosswind SST gradients[3,11–13].

The atmospheric response to SST fronts may significantly feed back onto the ocean[6]. Wind stress divergence and curl anomalies induced by SST fronts can generate Ekman pumping/suction, and thereby likely have effects on local flow and further feedback on large-scale circulation. The growth rate and wavelength of baroclinically unstable waves are significantly changed in response to SST-front induced wind stress curl anomalies feedback on ocean eddies[14]. The SST-front induced Ekman pumping in eddies is important in the extensions of western boundary current and in the Antarctic Circumpolar Current[15]. To examine the effects of mesoscale air-sea coupling on large-scale ocean circulation, Hogg and coauthors successfully used a first-order parameterized temperature-dependent wind stress scheme for mesoscale air-sea coupling in an idealized coupled model framework[16]. They found that the air-sea interaction alters the spatial and temporal scales of Ekman pumping, enhances the eddy kinetic energy, results in a weaker potential vor-

ticity barrier between the double gyre circulation, and then significantly reduces the strength of the nonlinear circulation near the western boundary. In a coastal upwelling system, there exists a significant impact of the air-sea coupling on both ocean mean circulation and eddy fields with implementation of an empirical SST-wind stress relationship in an idealized 2×2 km Regional Oceanic Modeling System (ROMS)[17].

The strong mesoscale air-sea coupling mainly occurs in regions where ocean fronts and eddies are active, such as the eastern tropical Pacific[1,18,19], the Southern Ocean[20,21], western boundary currents and their extension regions[6], and eastern boundary upwelling frontal zones[17,22]. The influences of the coupling can penetrate up to the free troposphere[23,24]. A number of factors contribute to the coupling[16]. Two widely cited physical mechanisms are the "vertical mixing mechanism"[25,26] and the "pressure adjustment mechanism"[27]. According to "vertical mixing mechanism", over warm SST, the air-sea heat flux tends to destabilize the atmosphere, increase mixing, and bring momentum downward to accelerate surface wind speed and stress. On the contrary, the atmosphere is stabilized over cool SST, and the surface is decoupled from aloft, decelerating surface winds. The "pressure adjustment mechanism" describes that atmospheric pressure changes resulting from air temperature and moisture changes in response to surface latent and sensible heat flux variations over SST fronts[27]. The resultant spatial pressure gradient will drive a secondary circulation[28]. Due to various mechanisms involved, the regression coefficient between wind stress and SST varies in each region, and so does the regression coefficient between wind stress divergence (curl) and downwind (crosswind) SST gradients. Surprisingly, the regression coefficients for the divergence are ubiquitously about twice as large as for the curl[21], despite the distinct governing physics[29]. This co-variation leads to the development of a temperature-dependent wind stress scheme to capture the essential dynamics of the process[16].

The previous study[11] investigated the ability of coupled climate models to capture the aforementioned positive correlation between SST and surface wind stress on oceanic mesoscale. They examined six climate models from the Intergovernmental Panel on Climate Change (IPCC) Fourth Assessment Report (AR4) and found that the wind stress in response to SST anomaly is already present due to vertical motion or convection in the atmosphere, but the magnitudes are at least a factor of 2 weaker than the observations, indicating a deficit in climate models. The performance of the mesoscale coupling with eddy-resolving and eddy-permitting ocean components in NCAR Community Climate System Model (CCSM) version 3.5 was investigated[30]. They noted that a more realistic pattern of positive correlation between SST and wind emerges over strong SST fronts and eddies in the eddy-resolving model than in the eddy-permitting model. Though the coupling is improved in terms of spatial distribution, the strength as measured by regression coefficients of wind stress and SST remains much weaker than observations, suggesting the shortcoming embedded in the coupled system.

In the work, we implement a simple temperature-dependent wind stress scheme[16] into NCAR Community Earth System Model (CESM) version 1.2.1 to enhance air-sea coupling. The scheme promotes the response of wind stress to the temperature difference between ocean and atmosphere, which often appears in the vicinity of meandering oceanic fronts due to the large disparity in the intrinsic variability scales in the ocean and atmosphere[7]. By conducting a series of three-year coupling experiments, we first select a proper coupling coefficient for the scheme to produce general agreement between the model and observations in terms of the statistical relationship between wind and SST. Afterwards, two 80-year simulations are conducted to examine the changes of ocean states in response to the air-sea coupling with/without the new scheme using the selected coefficient. Primarily, the purpose of this parameterization is to enhance mesoscale    (about 0.1° resolution) processes in a model of order 1° resolution.

The manuscript is organized as follows. Section 2 describes the model, the wind stress scheme, experimental design, and observational data for comparison. Section 3 presents the model results and their comparison. The underlying processes responsible for the changes are explored. Discussion and conclusions are given in section 4.

## 2. Methodology

### 2.1 Model description

The model used for this study is the NCAR Community Earth System Model version 1.2.1 (CESM1.2.1). This model supersedes version 4 of CCSM, including land and ocean biogeochemical models, an atmospheric chemistry

package, and a dynamic Greenland ice sheet model[31]. In the study, we disable the biogeochemical modules.

The atmospheric component model is the Community Atmosphere Model version 5 (CAM5). CAM5 has substantially revised physical parameterizations relative to CAM4[32,33]. Spectral element 1-degree grids are used for both atmospheric component and land component in the study.

The ocean component model is a primitive equation global ocean model, the Parallel Ocean Program version 2 (POP2[34]), with the hydrostatic and Boussinesq approximations. In the standard configuration, it has a zonal resolution of $1.2^o$ and varying meridional resolutions from $0.27^o$ at equator to $0.54^o$ at mid latitudes. There are 60 vertical levels, with 10-m resolution near the surface, gradually expanding to 250-m resolution at depth.

## 2.2 A temperature-dependent wind stress scheme

The bulk formula for ocean surface wind stress ($\vec{\tau}_s$) in the model is

$$\vec{\tau}_s = \rho C_D |\Delta \vec{U}| \Delta \vec{U} \qquad (1)$$

where $\rho$ is air density, $C_D$ is the drag coefficient, and $\Delta \vec{U} = \vec{U} - \vec{U}_o$ is the relative velocity between wind ($\vec{U}$) and surface currents ($\vec{U}_o$). The formula represents a quadratic increase of drag with wind[35]. In the study we allow the wind stress to depend upon the temperature difference between ocean ($T_o$) and atmosphere ($T_a$ at 2 m) in all ocean basins[16]. A correction to relative velocity speed (Eq. 1) is parameterized as below:

$$|\Delta \vec{U}|_{new} = (1 + \alpha(T_o - T_a)) |\Delta \vec{U}| \qquad (2)$$

where $\alpha$ is the coupling coefficient parameter to represent the strength of wind stress feedback. Subsequently, the wind stress is updated as

$$\vec{\tau}_s = \rho C_D |\Delta \vec{U}|_{new} \Delta \vec{U} \qquad (3).$$

Because of the change in wind stress, the surface latent heat flux ($Q_E$) and sensible heat flux ($Q_H$) are changed accordingly as:

$$Q_E = \lambda_v \cdot \rho C_E (q - q_{sat}(SST)) |\Delta \vec{U}|_{new}, \qquad (4)$$
$$Q_H = \rho c_p C_H (\theta - SST) |\Delta \vec{U}|_{new} \qquad (5)$$

where $\rho$ is the air density, $q$ is the specific humidity, $\lambda_v$ is the latent heat of evaporation, $C_E$ is a stability-dependent bulk transfer coefficient for evaporation, $c_p$ is the specific heat of air, $C_H$ is the sensible heat transfer coefficient, and $\theta$ is the ocean surface air temperature. Refer for formulations of these transfer coefficients[36]. To avoid including the effect of the temperature difference twice, the original $|\Delta \vec{U}|$ is used for the transfer coefficients.

## 2.3 Experimental design

In order to study the effects of SST front-induced surface wind feedback on ocean state estimates, we conduct two suites of numerical experiments (Table 1). The default 1850 preindustrial forcing is applied for all experiments[37]. The initial conditions for the 1850 simulation have been spun up by NCAR[38]. The first suite of experiments are run for three years to evaluate the sensitivity of the model to various wind stress feedback parameter $\alpha$. Here we allow $\alpha$ to vary from 0 to 0.1. The control experiment (Exp. CTRL) runs without the temperature-dependent wind stress (i.e. $\alpha$=0). The simulated wind stress and SST are averaged over a 4-month period for winter seasons in year 02 and 03. A box car average with dimensions $18^o \times 6^o$ (longitude $\times$ latitude) is applied to the model variables to obtain averages, and then these average are subtracted from the model variables to give high pass filtered variables. The spatially high-pass filter is similar to the $30^o \times 10^o$ (longitude $\times$ latitude) loess spatial high-pass filter[11,30]. The regression coefficients of high-pass-filtered wind stress and SST, wind stress divergence and downwind SST gradients, and wind stress curl and crosswind SST gradients are then compared against estimates from observations to obtain a reasonable value of $\alpha$ for the next long run. The second suite of two experiments is run for 80 years with and without the scheme. Considering the time required for ocean adjustment, the last 10-year output is averaged to examine the influence of the new scheme on ocean mean states. Output from year 21 to 80 is examined to explore the characteristics of El Niño Southern Oscillation (ENSO) in two simulations.

| Name | α | Time (yr) |
|---|---|---|
| Exp. CTRL | 0 | 3 |
| Exp. 01 | 0.015 | 3 |
| Exp. 02 | 0.03 | 3 |
| Exp. 03 | 0.05 | 3 |
| Exp. 04 | 0.1 | 3 |
| Exp. L01 | 0 | 80 |
| Exp. L02 | 0.03 | 80 |

**Table 1.** Numerical experiment lists.

## 2.4 Observational data for comparison of air-sea coupling strength

The application of the temperature-dependent wind stress is designed to strengthen the air-sea coupling within the marine atmospheric boundary layer (MABL). The coupling has appeared to be weak in NCAR CCSM3.5[30]. First, we compare the modeled linear relation of wind and SST with observations.

Surface wind stress is estimated from the NASA QuikSCAT satellite, which has been widely used to study the relation of wind stress and SST on the mesoscale[1,11]. QuikSCAT winds are available from August 1999 to December 2009 with approximately a quarter degree resolution, downloaded from ftp://ftp.remss.com/qscat/bmaps_v04/. Wind stress is calculated based on the well developed bulk formula[40].

SST fields are from the Advanced Very High Resolution Radiometer (AVHRR) in the NOAA satellite information system (ftp://eclipse.ncdc.noaa.gov/pub/). The data used has $0.25^o \times 0.25^o$ horizontal resolution from year 2000 to 2009.

For comparison to model solutions, we averaged the QuikSCAT wind stress and AVHRR SST over the 4-month period of November-February for boreal winter, and the 4-month period of May-August for austral winter from year 2000 to 2009. The box car average with dimensions $18^o \times 6^o$ (longitude × latitude) is applied to SST, wind stress, wind stress divergence and curl.

# 3. Results
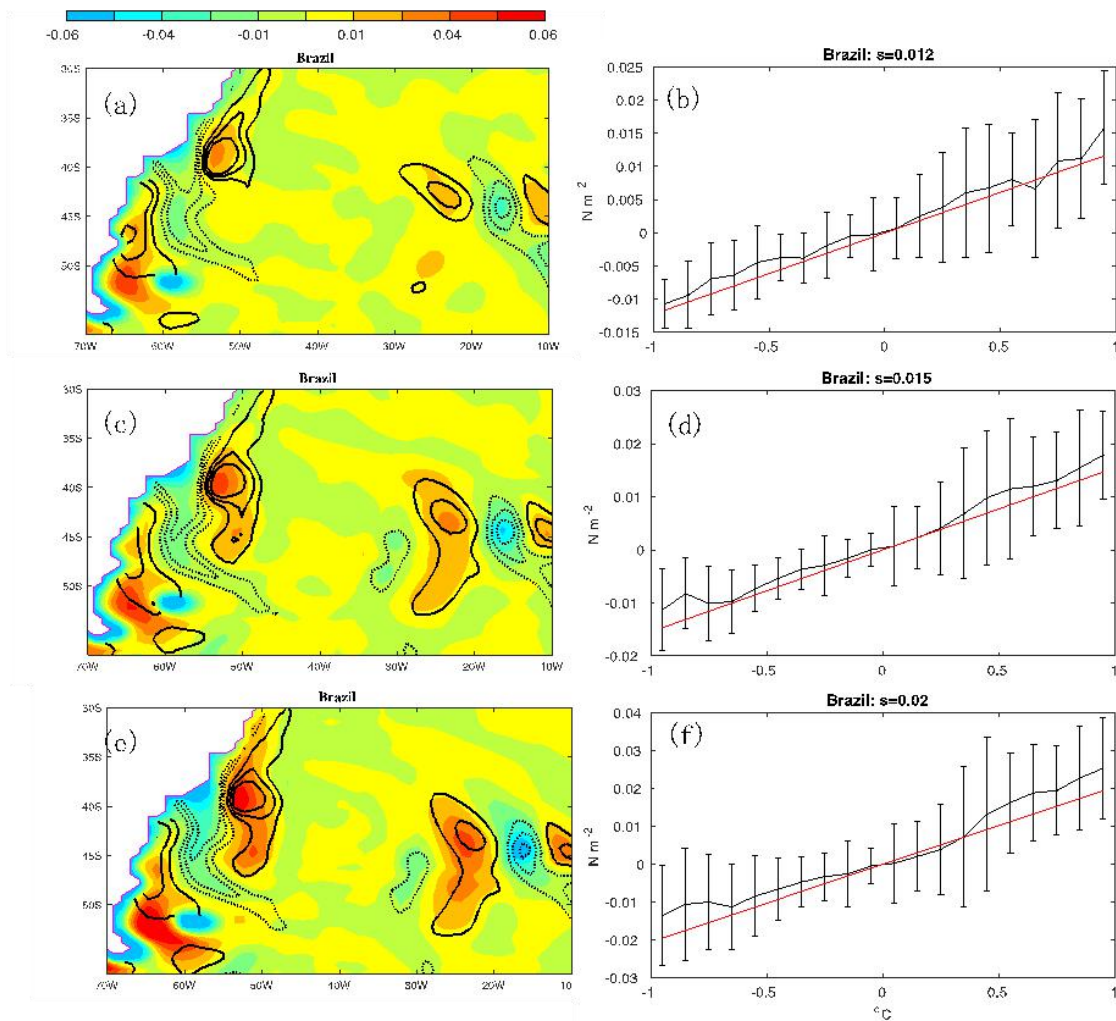
**Figure 1.** Spatially high-pass-filtered wind stress (τ, colors) and SST (contours) averaged from November – February of year 02-03 (upper), and bin scatterplots (lower) within the Brazil current region from Exp. CTRL (a-b), Exp.02 (c-d), and Exp. 04 (e-f). The red lines indicate the linear regression, and s denotes the regression coefficient. The error bars are ±1 standard deviation of the means within each bin.

## 3.1 Three-year run case

To quantify the strength of the mesoscale air-sea interaction, we estimate the magnitudes of regression coefficients between high-pass-filtered wind stress and SST in wintertime by constructing binned scatterplots. The relation in wintertime is explored, because wind stress and SST fields are more energetic in winter than in summer in the middle latitudes, as shown in the previous study[11]. Wind stress is binned by SST perturbations of every 0.1 degree in the western boundary current separation regions. **Figure 1** shows high-pass-filtered wind stress and SST in the Brazil-Malvinas confluence, where positive linear trends between wind stress and SST are noted in both observations and models. The slope of the linear regression (estimated from a least-squares fit) from observations is 0.015, consistent with previous findings[21]. The slopes increase from 0.012 of Exp. CTRL (**Figure 1**b) to 0.013 of Exp. 01, 0.015 of Exp. 02 (**Figure 1**d), 0.016 of Exp. 03 and 0.020 of Exp. 04 (**Figure 1**f). The coupling between wind and SST continuously increases with α in major western boundary current regions (**Figure 2**).
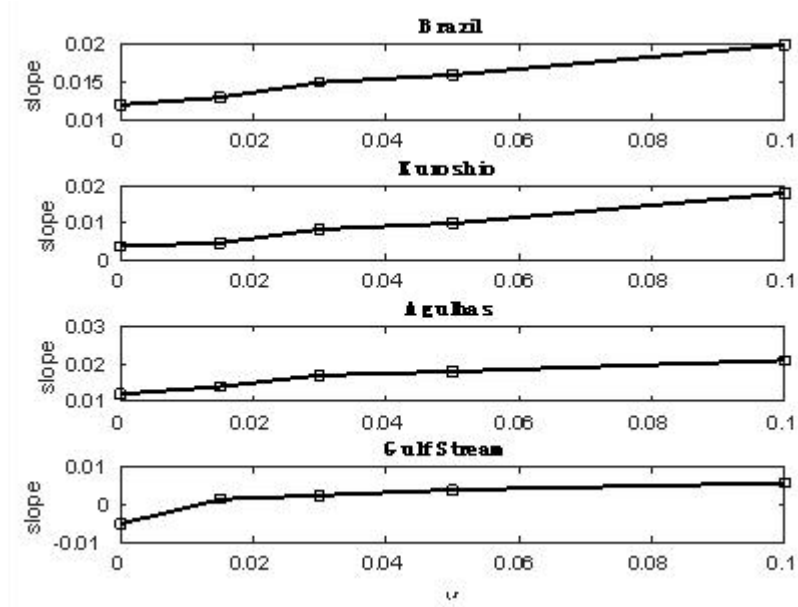
**Figure 2.** Slopes estimated from wind stress and temperature anomalies in the Brazil region, the Kuroshio region, the Agulhas region and the Gulf Stream region.

The high-pass-filtered wind stress curl ($\nabla \times \vec{\tau}$, N m$^{-3}$ per 10,000 km) and crosswind SST gradient ($\nabla T \times \vec{\tau}$, $^\circ$C per 100 km), as well as wind stress divergence ($\nabla \cdot \vec{\tau}$, N m$^{-3}$ per 10,000 km) and downwind SST gradient ($\nabla T \cdot \vec{\tau}$, $^\circ$C per 100 km) are analyzed following the same aforementioned procedure, where T denotes SST, $\tau$ is the wind stress, and $\vec{\tau}$ denotes the unit vector in the direction of the surface wind stress. The positive regression coefficients are obtained. In the Agulhas return current region, the observed coefficient of high-pass-filtered $\nabla \times \vec{\tau}$ and $\nabla T \times \vec{\tau}$ is about 1.22 averaged from year 2000 to 2009, consistent with previous findings[11]. **Figure 3** shows the increase of positive coefficients with α from Exp. CTRL (s=0.86), Exp. 02 (s=1.2) to Exp. 04 (s=1.4). Exp.02 obtains the closest regression coefficient to the observations. The spatial distributions of $\nabla \times \vec{\tau}$ and $\nabla T \times \vec{\tau}$ illustrate that the perturbation fields of both ocean and atmosphere are enlarged with α (**Figure 4**). In the Gulf Stream region, the observed coefficient of high-pass-filtered $\nabla \cdot \vec{\tau}$ and $\nabla T \cdot \vec{\tau}$ is 1.5, and the coefficients are 0.81, 1.6 and 7.7 from Exp. CTRL, Exp.02 and Exp. 04, respectively. Again, Exp.02 obtains the closest regression coefficient to the observations.
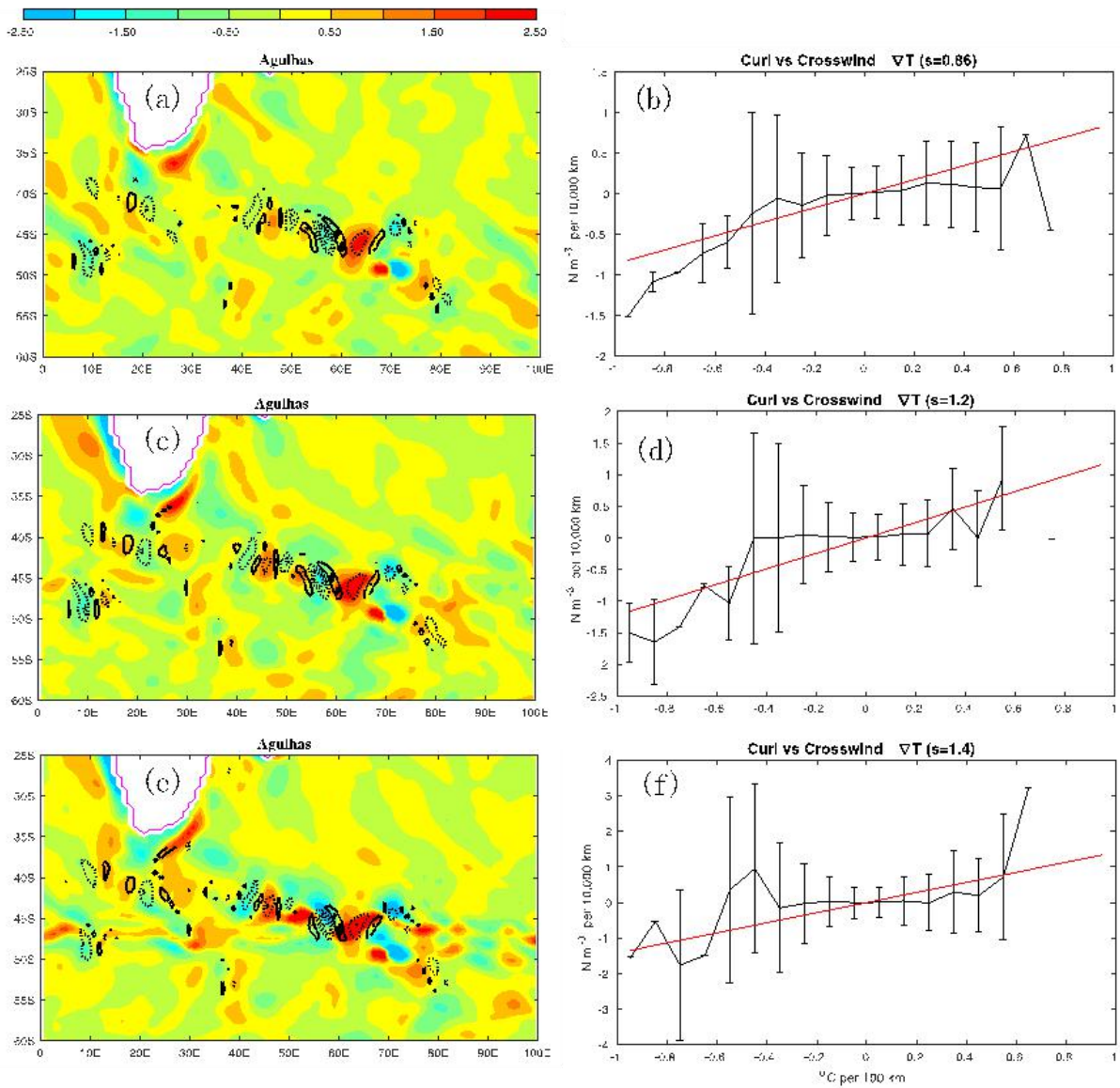
**Figure 3.** Spatially high-pass-filtered wind stress curl ($\nabla \times \vec{\tau}$, colors) and crosswind SST gradient ($\nabla T \times \vec{\tau}$, contours) averaged from May – August of year 03 (left), and bin scatterplots (right) within the Agulhas region from Exp. CTRL (a-b), Exp.02 (c-d) and Exp. 04 (e-f). The red lines indicate the linear regression, and s denotes the regression coefficient. The error bars are ±1 standard deviation of the means within each bin.
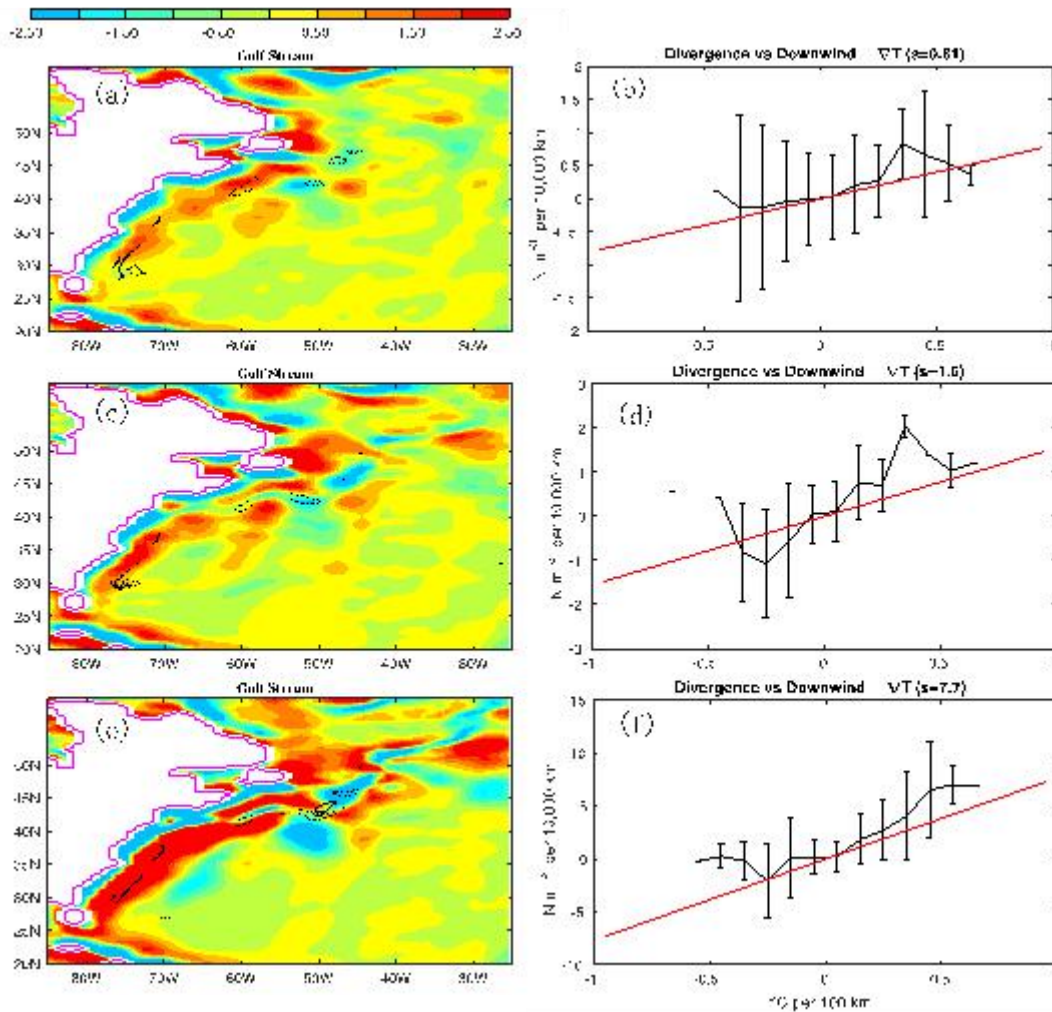
**Figure 4.** Spatially high-pass-filtered wind stress divergence ($\nabla \cdot \vec{\tau}$, colors) and downwind SST gradient ($\nabla T \cdot \vec{\tau}$, contours) averaged from November – February of year 02-03 (left), and bin scatterplots (right) within the Gulf Stream region from Exp. CTRL (a-b), Exp.02 (c-d), and Exp. 04 (e-f). The red lines indicate the linear regression, and s denotes the regression coefficient. The error bars are ±1 standard deviation of the means within each bin.

Thus, Exp. 02 tends to be sufficiently close to observations in terms of air-sea coupling strength, while the spatial structure remains less energetic than the real world due to the coarse model resolution. In the next section, we will explore the effects of implementation of the simple scheme with α=0.03 in an 80-year run. α=0.03 may not be the best choice, but the strengthening of the air-sea coupling by the simple parameterization is evident, and it is useful to test the change of ocean induced by the scheme.

## 3.2 Eighty-year run case

The influence of the temperature-dependent wind stress on ocean mean states, by comparing SST, surface currents, and zonal currents at equatorial Pacific from the two model simulations is examined via comparisons of Exp. L01 and Exp. L02. The model solutions are averaged over the last 10 years for the following comparisons, except for the estimates of Niño-3.4 index. Even though the deep ocean of both coupled models have not reached equilibrium in 80 years, we focus on the upper ocean and fast processes in response to wind change, such as SST, vertically integrated (barotropic) transport, and equatorial processes.

a. SST

In general, the SST distributions from Exp. L01 and Exp. L02 agree with Levitus climatological distributions[38]. Comparing to Exp. L01, the global-averaged mean SST bias in Exp. L02 reduces about 0.1 ℃, approximate 23% of SST bias in Exp. L01 (-0.43 ℃). Meanwhile, the root mean square error (RMSE) in Exp. L02 decreases about 0.14 ℃

relative to Exp. L01. The spatial maps of SST biases in the two experiments are compared in **Figure 5**a and 5b. It has been well known that the CESM has warm biases near the eastern boundary of Pacific Ocean[39]. In the subtropical southeast Pacific (SEP), the warm biases are apparent in Exp. L01, while the biases are reduced by about 0.5-1.0°C in Exp. L02 (Fig. 5a-b). The cold bias in the central North Pacific and eastern South Indian is reduced by about 0.5-1.0°C. In the Pacific sector of the Southern Ocean, the warm bias in Exp.L01 is reduced as well. But there is no clear improvement in the subpolar North Atlantic where deep convection is dominant. And there is no clear improvement at 500 m as well (**Figure 5**c and 5d), since the scheme is only effective near ocean surface.
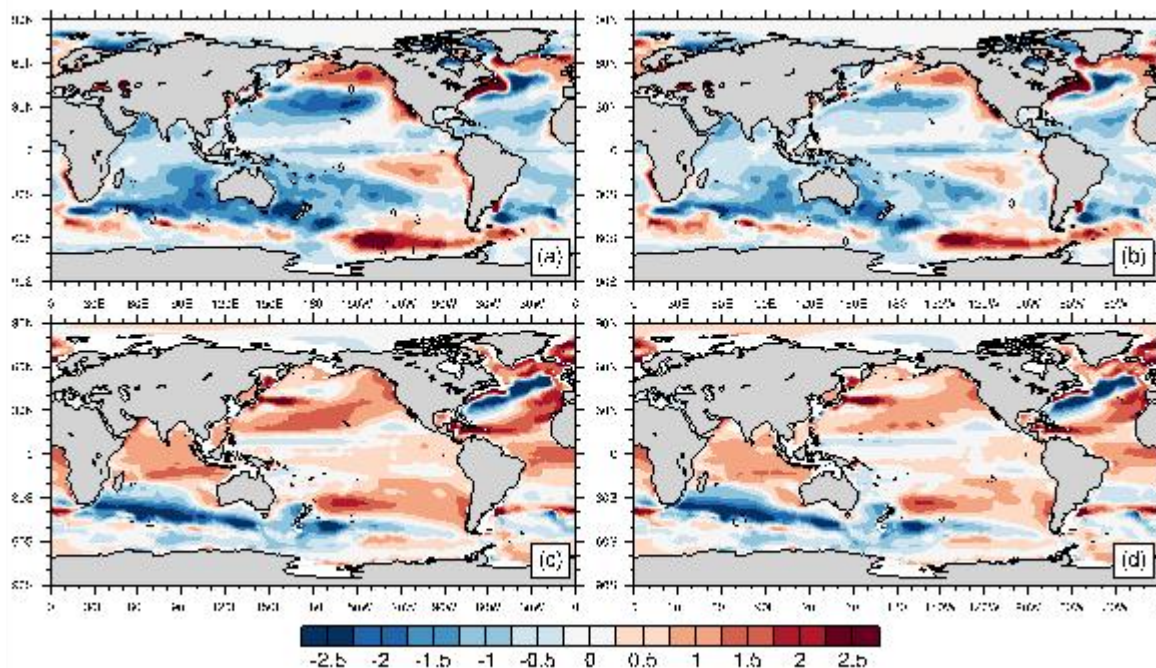


**Figure 5.** Temperature differences between LEVITUS climatology[38] and 10-year model mean at 5 m (a, b), and 500 m (c, d) from Exp. L01 (left) and Exp.L02 (right).

**Figure 6** compares the variations in wind stress, surface currents and heat flux in Exp. L02 relative to Exp. L01. SST differences between Exp. L02 and Exp. L01 can be identified in all ocean basins (**Figure 6**b,c). These differences can be induced by either change of surface heat flux (**Figure 6**d) or change of momentum flux, such as Ekman response, mixing and advection with ocean circulations (**Figure 6**b,c). Near the eastern boundary of the Pacific Ocean, heat flux differences are negligible. The temperature reduction in the equatorial Pacific and along South America coast is not in response to heat flux variations. Rather, the strengthening of the upwelling favorable winds dominates the local temperature change (**Figure 6**a-c). The offshore surface currents further expand the cooling of the SEP in Exp. L02. It is evident that the modified wind stress tends to reduce the warm bias (**Figure 5**a), consistent with previous findings that the warm SST biases are mainly due to deficiencies in air-sea coupling[39]. In the central North Pacific and the North Atlantic, the temperature is higher in Exp. L02 than Exp. L01, due in part to the enhanced convergence of surface wind stress (**Figure 6**b) and anticyclonic circulation in Exp. L02 (**Figure 6**c). In the eastern South Indian, the enhanced southwestward flow from equator (**Figure 6**c) advects warm water and reduces the cold bias. The flow is enhanced presumably due to the enhanced easterly in the tropical Pacific (**Figure 6**b). Since the change in heat flux (**Figure 6**d) is spatially different with the change of SST (**Figure 6**b), the change in momentum flux fields is more dominant.
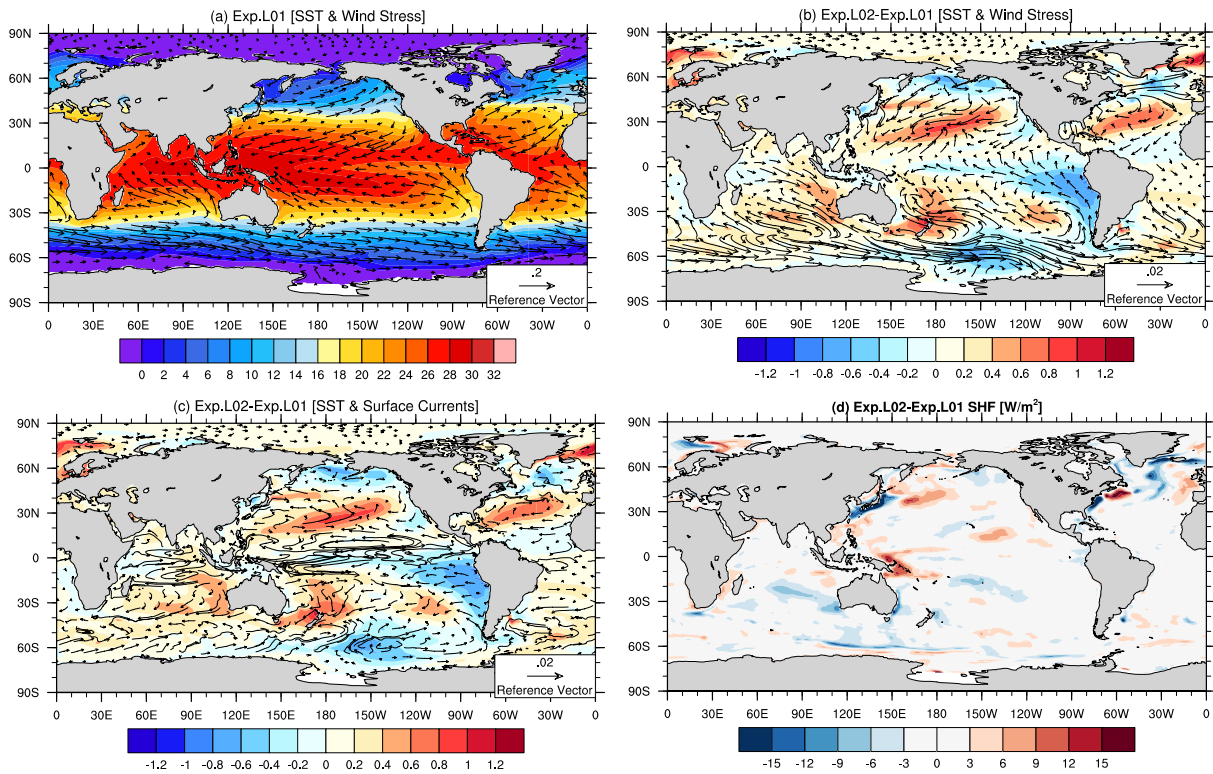
**Figure 6.** 10-year averaged SST in ºC (color) and wind stress in N m$^{-2}$ (vectors) from Exp. L01 (a), their differences between Exp. L02 and Exp.L01 (b), differences in surface currents (m s$^{-1}$) and SST (c), and differences in surface heat flux (W m$^{-2}$) (d). Positive values mean ocean gain heat, and vice versa.

b. Barotropic stream function (BSF)

The barotropic stream function represents the ocean large-scale circulation. **Figure 7** shows the BSF distributions from Exp. L02 and their differences from Exp. L01. The BSF distributions of Exp. L02 are very similar to those of the present-day simulations of CCSM4[39] in response to large-scale wind stress curls. Close to western boundary separation regions, Exp. L02 exhibits weakening of gyre circulations in both the Pacific and Atlantic Ocean, probably induced by the temporal variations of wind stress, consistent with previous findings[16].

Particularly, the ACC transport is weakened as well. It has long been known that NCAR climate model tends to overestimate the Drake Passage transport[39]. In Exp. L02, weakened wind stress over ACC (**Figure 7**b) shallows isopycnals, and reduces transport due to thermal wind balance. Meanwhile, enhanced wind perturbations (**Figure 4** and 6b) leads to stronger eddy activity, acting to flatten isopycnals out, and subsequently reducing the transport as well. Consequently, the reduction of ACC transport reduces the coupled model biases.
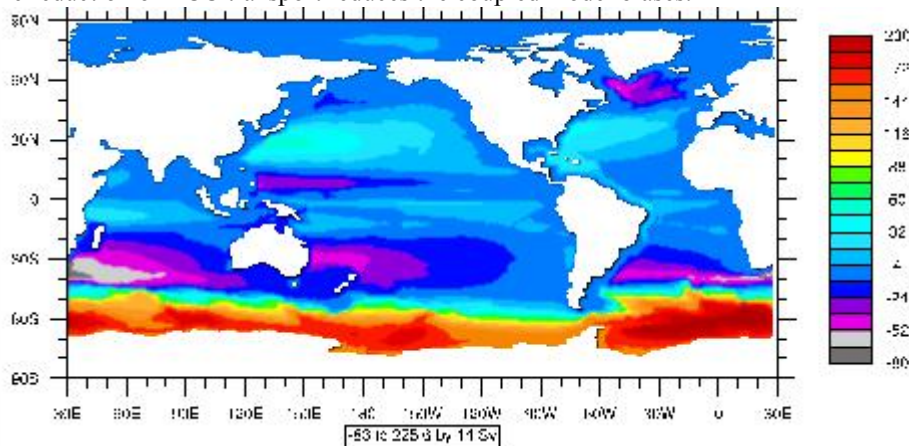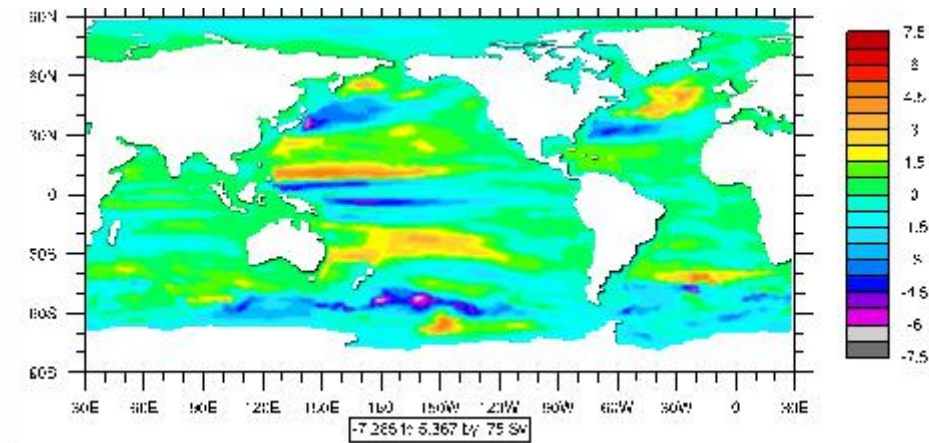
**Figure 7.** Barotropic stream function (BSF) from Exp. L02 (top) and its difference with Exp. L01 (bottom) averaged over year 71-80. Positive (negative) values denote clockwise (counterclockwise) circulations.

## c. Equatorial Pacific
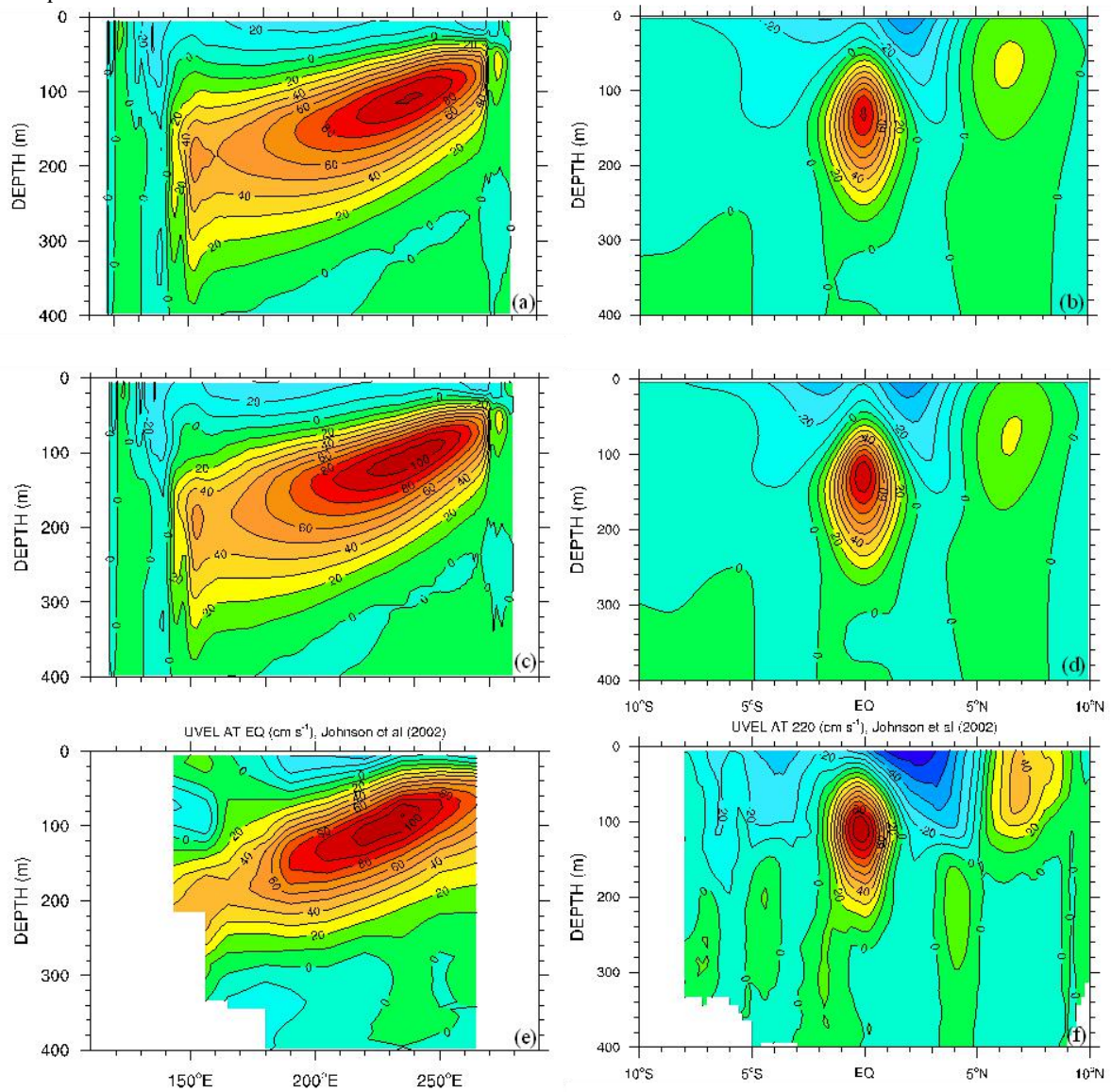


**Figure 8.** Averaged zonal velocity in the Pacific Ocean along the equator (left) and at 220°E (right) from Exp. L01 (a,b), Exp. L02 (c,d), and observations[41] (e,f). The contour interval is 10 cm s⁻¹.

In the equatorial Pacific Ocean, zonal currents along the equator and at 220° E from Exp. L01 and Exp. L02 are

compared to the observations[41]. In general, the complex equatorial current system, including Equatorial Undercurrent (EUC), South Equatorial Current (SEC) and North Equatorial Counter Current (NECC), is well represented in both model solutions (**Figure 8**), consistent with CCSM4 results[39]. In terms of the core depth (the depth of the maximum zonal velocity) and strength of EUC, Exp. L02 is in better agreement with observations than Exp. L01. Exp. L02 shows a stronger westward SEC south of the equator than Exp. L01, more consistent with observational data[41] (**Figure 8**b, d&f). However, an asymmetric SEC, with stronger westward flow north of the equator, is underestimated in both simulations. This is likely induced by more symmetric-than-observed wind/precipitation forcing problems in these coupled simulations[38]. In addition, the NECC at about 5-10 °N is slightly weakened in Exp. L02, due to the weakened trade winds there (**Figure 6**b).

d. Niño-3.4 index

Besides the differences in estimates of ocean mean states from the two experiments, we also examine Niño-3.4 index, the area-averaged monthly SST anomalies (5°N-5°S, 170°-120°W), associated with the ENSO variability. **Figure 9** compares the observed variance of Niño-3.4 index (https://www.ncdc.noaa.gov/, 1871-2015) with those from Exp. L01 and Exp. L02, estimated over year 21-80. Generally, both observed warm and cold ENSO events have the tendency to peak near the end of the calendar year. The seasonal cycles of both experiments reach maximum in January and minimum in June, similar to the behavior of CCSM4[42]. The variation range from Exp. L01 is similar to CCSM4 as well, much stronger than the observed variations. In contrast, the variations from Exp. L02 are weakened by ~30%, much closer to observations. **Figure 10** compares spatial maps of SST standard deviations in the tropical Pacific from Exp. L01 and Exp.L02. The magnitude of the SST variability over the eastern tropical Pacific in Exp. L02 has been reduced.
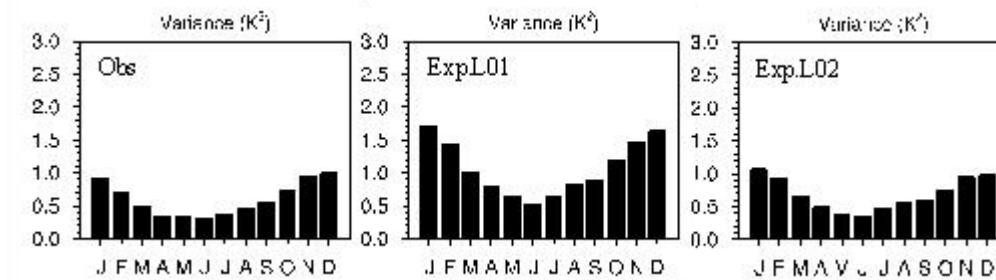


**Figure 9.** Monthly variance of the Nino-3.4 SST index from observations, Exp. L01 and Exp. L02 estimated over year 21-80.
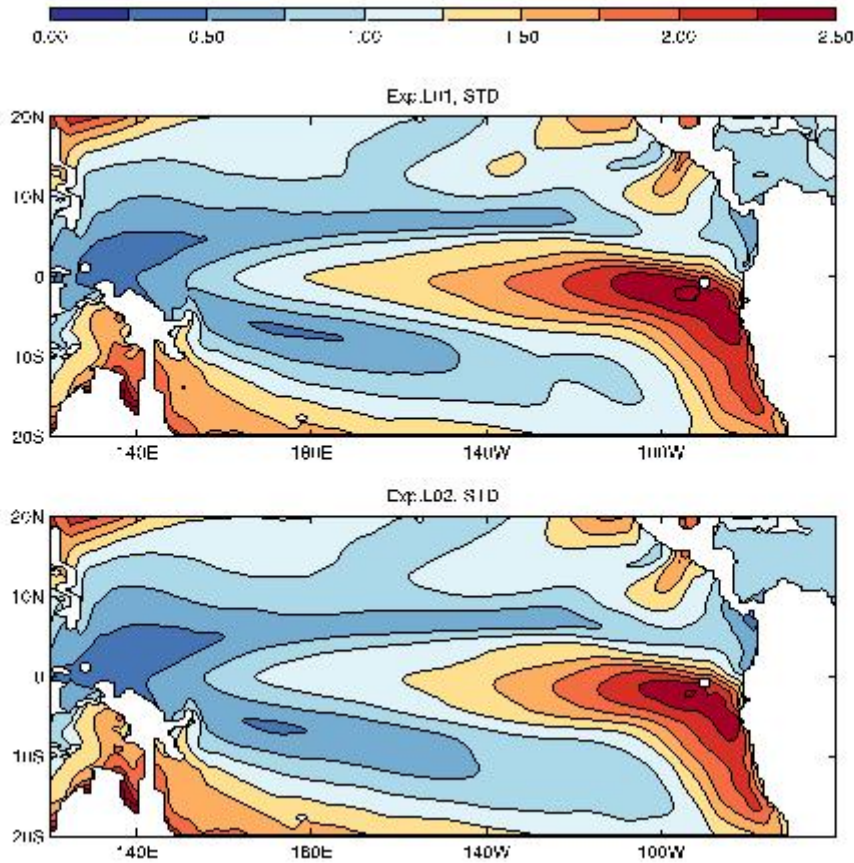
**Figure 10.** Standard deviation maps of SST from Exp. L01 (top) and Exp.L02 (bottom).

The wavelet power spectrum of Niño-3.4 index from observation, Exp. L01 and Exp. L02 is compared in **Figure 11** to examine the temporal variability. Exp. L01 exhibits a single sharp peak in the 3-6 year band, consistent with CCSM4 characteristics, while that of Exp. L02 has a double peak spanning a broader range of 3-8 year, more consistent with 3-9 year range found in observations. Noticeably, even though the power of Exp. L02 has reduced, it is still larger than that from observations.

The improvements of ENSO variability and magnitude in Exp. L02 are probably induced by the reduction of SST bias in the SEP and enhancement of southeast trades, as shown in **Figure 5** and **Figure 6.** A previous study[43] systematically analyze the impact of the warm SST bias in the SEP on ENSO variability and prediction. Their results show that the correction of ocean mean state in a coupled general circulation model (GCM) can reduce ENSO magnitude and refine ENSO frequency. In addition, the eastern equatorial Pacific is one of the most active mesoscale air-sea coupling regions due to the existence of TIWs. By explicitly parameterizing TIWs in a coupled GCM, Imada and Kimoto[44] illustrate that the air-sea interaction of TIWs can modulate ENSO variability as well.
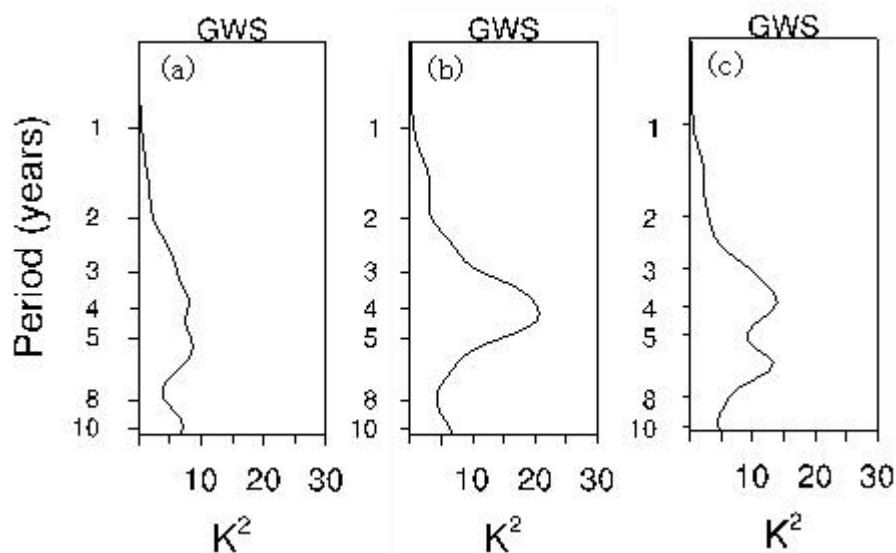
**Figure 11.** The global wavelet spectrum (GWS) of Niño-3.4 SST index from observation (a), Exp. L01 (b) and Exp. L02 (c) estimated over year 21-80.

## 4. Conclusions and Discussion

A simple temperature-dependent wind stress scheme is implemented into NCAR CESM1.2.1 to enhance positive wind and SST correlations over SST frontal regions within a relative coarse ocean component. The study is an attempt to strengthen this mesoscale air-sea coupling feedback on large-scale oceans in a state-of-the-art climate model. Improvements of ocean simulation are identified with the introduction of the scheme. The results show that the new scheme improves the positive correlation between SST and wind stress near the western boundary currents. The surface heat flux and wind stress are refined, and consequently, the global SST biases are reduced. The vertically integrated transport for gyre circulations shows variations consistent with the previous process study[16]. The SEC is strengthened in the equatorial Pacific current system, more consistent with observations. The Niño-3.4 index with the new scheme exhibits improvements of ENSO magnitude and variability.

Compared to the high-resolution CESM[30], the scheme is capable to enhance the coupling coefficients, but not as good as the high-resolution model in terms of the spatial structure. With increased ocean model resolution and improvements in MABL parameterizations, the mesoscale air-sea coupling would be better represented[45]. As pointed out in a previous study[30], the air-sea coupling in the eddy-resolving CCSM was still weaker than observations. The scheme might be useful for strengthening the air-sea coupling at high resolution, but the coupling coefficient should be thoroughly tested in different models and at different resolutions.

Furthermore, the study focuses on ocean response, and has not investigated the atmospheric response to the coupling. The atmospheric response to fronts and eddies has been an area of rich studies in many regions, such as the Aughlas current[21], the Gulf Stream[24], the eastern Equatorial Pacific[8], and so on. The global atmospheric response to the scheme will be explored in the future.

## Author Contributions

F. Xu designed, implemented, analyzed and wrote up the study.

## Conflict of Interest

No conflict of interest.

## Acknowledgements

# References

1.  Chelton DB, Coauthors. Observations of coupling between surface wind stress and sea surface temperature in the eastern tropical Pacific. Journal of Climate 2001; 14: 1479–1498.
2.  O'Neill LW, DB Chelton, SK Esbensen. Observations of SST-induced perturba- tions of the wind stress field over the Southern Ocean on seasonal timescales. Journal of Climate 2003; 16(2): 340–2,354.
3.  Chelton DB, MG Schlax, MH Freilich, *et al*. Satellite radar measurements reveal short-scale features in the wind stress field over the world ocean. Science, 2004; 303: 978–983.
4.  Xie SP. Satellite observations of cool ocean-atmosphere interaction. Bulletin of the American Meteorological Society (BAMS) 2004, 85: 195–208.
5.  Park KA, PC Cornillon, DL Codiga. Modification of surface winds near ocean fronts: Effects of Gulf Stream rings on scat- terometer (QuikSCAT, NSCAT) wind observa- tions. Geophysical Research Letters 2006; 111: C03021.
6.  Small RJ, SP deSzoeke, SP Xie, *et al*. Air-sea interaction over ocean fronts and eddies. Dynamics of Atmospheres and Oceans 2008; 45: 274–319.
7.  Chelton DB, SP Xie. Coupled ocean-atmosphere interaction at oceanic mesoscales. Oceanography 2010; 23(4): 52–69.
8.  Zhang RH, Z Li, J Zhu, *et al*. Impact of tropical instability waves-induced SST forcing on the atmosphere in the tropical Pacific, evaluated using CAM5.1, Atmospheric Science Letters 2014.
9.  Ma X, Coauthors. Western boundary currents regulated by interaction between ocean eddies and the atmosphere. Nature 2016; 535: 533–537.
10.  Gemmrich J, A Monahan. Covariability of near-surface wind speed statistics and mesoscale sea surface temperature fluctuations. Journal of Physical Oceanography 2018; 48(3): 465-478.
11.  Maloney ED, DB Chelton. An assessment of the sea surface temperature influence on surface wind stress in numerical weather prediction and climate models. Journal of Climate 2006; 19(2): 743–2,762.
12.  Song Q, DB Chelton, SK Esbensen, *et al*. Coupling between sea surface temperature and low-level winds in mesoscale numerical models. Journal of Climate 2009; 22: 146–164.
13.  Kilpatrick T, N Schneider, B Qiu. Boundary layer convergence induced by strong winds across a Midlatitude SST Front. Journal of Climate 2014; 27: 1698–1718.
14.  Spall AM. 2007. Effect of Sea Surface Temperature–Wind Stress Coupling on Baroclinic Instability in the Ocean. Journal of Physical Oceanography 2014; 37(4): 1092-1097.
15.  Gaube P, Chelton DB, Samelson RM, *et al*. Satellite Observations of Mesoscale Eddy-Induced Ekman Pumping. Journal of Physical Oceanography 2015; 45(1):104-132.
16.  Hogg A, WK Dewar, P Berloff, *et al*. The Effects of Mesoscale Ocean–Atmosphere Coupling on the Large-Scale Ocean Circulation. Journal of Climate 2009; 22: 4066–4082.
17.  Jin X, C Dong, J Kurian, *et al*. SST–wind interaction in coastal upwelling: Oceanic simulation with empirical coupling. Journal of Physical Oceanography 2009; 39: 2957–2970.
18.  Small RJ, SP Xie, Y Wang. Numerical simulation of atmospheric response to Pacific tropical instability waves. Journal of Climate 2003; 16: 3723–3741.
19.  Zhang RH, 2014. Effects of tropical instability wave (TIW) - induced surface wind feedback in the tropical Pacific Ocean. Climate Dynamics 2012; 42: 467-485.
20.  O'Neill LW, Chelton DB, Esbensen SK, *et al*. High-resolution satellite measurements of the atmospheric boundary layer response to SST variations along the Agulhas Return Current. Journal of Climate 2005; 18: 2706–2723.
21.  O'Neill LW, DB Chelton, SK Esbensen. Covariability of surface wind and stress responses to sea-surface temperature fronts. Journal of Climate 2012; 25: 5916–5942.
22.  Chelton DB, MG Schlax, RM Samelson. Summertime coupling between sea surface temperature and wind stress in the California Current System. Journal of Physical Oceanography 2007, 37: 495–517.
23.  Feliks Y, M Ghil, E Simonnet. Low-frequency variability in the midlatitude atmosphere induced by an oceanic thermal front. Journal of the Atmospheric Sciences 2004; 61: 961–981.
24.  Minobe S, Kuwano-Yoshida A, Komori N, *et al*. Influence of the Gulf Stream on the troposphere. Nature, 2008; 452: 206–209.
25.  Hayes SP, McPhaden MJ, Wallace JM. The influence of sea surface temperature on surface wind in the eastern equatorial Pacific: Weekly to monthly variability. Journal of Climate 1989; 2: 1500–1506.
26.  Wallace J, T Mitchell, C Deser. The influence of sea-surface temperature on surface wind in the eastern equatorial Pacific: Seasonal and interannual variability. Journal of Climate 1989; 2: 1492–1499.
27.  Lindzen RS, Nigam S. On the role of sea surface temperature gradients in forcing low level winds and convergence in the tropics. Journal of the Atmospheric Sciences 1987; 44: 2418–2436.
28.  Wai MMK, Stage SA. Dynamical analyses of marine atmospheric boundary layer structure near the Gulf Stream oceanic front. Quarterly Journal of the Royal Meteorological Society 1989; 115: 29–44.
29.  Schneider N, B Qiu. The atmospheric response to weak sea surface temperature fronts. Journal of the Atmospheric Sciences 2015; 72: 3356-3377.
30.  Bryan FO, R Tomas, JM Dennis, *et al*. Frontal scale air–sea interaction in high-resolution coupled climate models.

Journal of Climate 2010; 23: 6277–6291.

31. Hurrell JW, coauthors. The Community Earth System Model: A Framework for Collaborative Research. Bulletin of the American Meteorological Society (BAMS) 2013; 94: 1339–1360.

32. Gettelman A, Coauthors. Global simulations of ice nucleation and ice supersaturation with an improved cloud scheme in the Community Atmosphere Model. Journal of Geophysical Research 2010; 115: D18216.

33. Neale RB, Coauthors. Description of the NCAR Community Atmosphere Model (CAM5.0). NCAR Tech. 2010. Note NCAR/TN-486+STR, 268 pp.

34. Smith RD, Coauthors. The Parallel Ocean Program (POP) reference manual, ocean component of the Community Climate System Model (CCSM). Los Alamos National Laboratory Tech. Rep. LAUR-10-01853 2010; 141.

35. Large WG, SG Yeager. The global climatology of an interannually varying air-sea flux data set. Climate Dynamics 2009; 33: 341-364.

36. Large WB. Surface fluxes for practitioners of global ocean data assimilation. In: Chassignet E.P., Verron J. (eds) Ocean Weather Forecasting. Springer, Dordrecht 2006; 229-270.

37. Gent PR, G Danabasoglu, LJ Donner, et al. The Community Climate System Model Version 4 Journal of Climate 2011; 24: 4973–4991.

38. Levitus S, Boyer T, Conkwright M, et al. Introduction, vol 1. World Ocean Database 1998, NOAA Atlas NESDIS 1998; 18: 346.

39. Danabasoglu G, SC Bates, BP Briegleb, S. et al. The CCSM4 ocean component. Journal of Climate 2012; 25: 1361–1389.

40. Large WG, S Pond. Sensible and latent-heat flux measurements over the Ocean. Journal of Physical Oceanography 1982; 12(5): 464-482.

41. Johnson G, B Sloyan, W Kessler, et al. Direct measurements of upper ocean currents and water properties across the tropical Pacific during the 1990s. Progress in Oceanography 2002; 52: 31–61.

42. Deser C, AS Phillips, RA Tomas, et al. ENSO and Pacific decadal variability in the community climate system model version 4. Journal of Climate 2012; 25: 2622–2651.

43. Manganello JV, B Huang. The influence of systematic errors in the Southeast Pacific on ENSO variability and prediction in a Coupled GCM. Climate Dynamics 2009.

44. Imada Y, M Kimoto. Parameterization of tropical instability waves and examination of their impact on ENSO characteristics. Journal of Climate 2012; 25: 4568–4581.

45. Kirtman, BP, Bitz C, Bryan F, et al. Impact of ocean model resolution on CCSM climate simulations. Climate Dynamics 2012; 39: 1303.